



Generalized orbital angular momentum symmetry in parametric amplificationR. B. Rodrigues , G. B. Alves, R. F. Barros , C. E. R. Souza, and A. Z. Khoury
Instituto de Física, Universidade Federal Fluminense, 24210-346 Niterói, RJ, Brazil

(Received 23 September 2021; accepted 23 December 2021; published 6 January 2022)

We investigate interesting symmetry properties verified by the down-converted beams produced in optical parametric amplification with structured light. We show that the Poincaré sphere symmetry, previously demonstrated for first-order spatial modes, translates to a multiple Poincaré sphere structure for higher orders. Each one of these multiple spheres is associated with a two-dimensional subspace defined by a different value of the orbital angular momentum. Therefore, the symmetry verified by first-order modes is reproduced independently in each subspace. This effect can be useful for parallel control of independently correlated beams.

DOI: [10.1103/PhysRevA.105.013510](https://doi.org/10.1103/PhysRevA.105.013510)**I. INTRODUCTION**

Optical parametric amplification is a powerful tool for generating quantum correlations between independent light beams [1–6]. It has been used as an important resource for many quantum applications such as quantum teleportation [7] and quantum metrology [8]. The longitudinal-mode structure of quantum correlated beams generated by an optical parametric oscillator gives rise to a frequency comb of quadrature entangled beams that are good candidates to scalable quantum computers [9–11]. These useful correlations stem from different constraints imposed by the parametric process, which includes energy and momentum conservation among the photons participating in the nonlinear interaction. Transverse momentum conservation is in the heart of well-established spatial correlations between the photons emitted by spontaneous parametric down-conversion [12]. These spatial correlations can be combined with polarization entanglement [13], giving rise to hyperentangled two-photon quantum states [14–17].

Interesting conditions are also verified when structured light beams are coupled in the parametric process. Orbital angular momentum (OAM) conservation has been investigated in cavity-free spontaneous [18] and stimulated [19] parametric down-conversion. The nonlinear coupling between different transverse modes is subject to conditions imposed by the spatial overlap between them, giving rise to selection rules that limit the modes allowed in the interaction [20–23]. When the process is intensified inside an optical resonator, cavity conditions also dictate which modes can survive the loss-gain balance, which can affect both the transverse [24–26] and longitudinal [27] mode structures. These effects determine whether OAM can be exchanged between the interacting modes [28–31]. The selection rules that apply to parametric amplification also lead to symmetry properties that have already been investigated for first-order modes. In particular, OAM conservation and intensity overlap between the down-converted beams were shown to impose a reflection symmetry in the Poincaré sphere representation of the signal and idler beams [32–35]. OAM correlations inside an optical

parametric oscillator (OPO) give rise to entanglement in the continuous variable regime [36], that can be combined with polarization to produce continuous variable hyperentanglement [37–41].

In this work, we investigate how this Poincaré sphere symmetry extends to multiple higher orders, simultaneously amplified in the OPO cavity. In principle, this subject suggests a difficult task, since higher-order modes do not have a simple geometric representation. However, the selection rules that arise from the spatial overlap between the interacting modes impose restrictions that limit the symmetry properties to two-dimensional subspaces of the higher-order mode structure. These subspaces are spanned by pairs of modes with opposite OAM values. The Poincaré symmetry is independently verified inside each subspace, what can be useful for parallel control of independent down-conversion channels. Here, we will focus on the classical behavior of the mode dynamics, which will serve as a starting point for a future investigation in the quantum domain. As we will see, this classical instance of the problem already encompasses a rich dynamics.

II. STRUCTURED LIGHT INJECTION IN PARAMETRIC AMPLIFICATION

Let us consider the optical parametric amplification process involving two input beams, *pump* and *signal*, which interact through a nonlinear crystal and generate a third beam called *idler*. The interacting beams carry the frequencies ω_p (pump), ω_s (signal), and ω_i (idler), satisfying $\omega_p = \omega_s + \omega_i$. The three-beam interaction is mediated by the second-order nonlinear susceptibility of the crystal. We are interested in deriving general symmetry properties carried by the signal and idler beams as a result of the nonlinear coupling. This kind of symmetry has already been investigated, both theoretical [33] and experimentally [34], for first-order modes, where OAM conservation and intensity overlap were the main features behind the symmetry observed. Our objective is to extend these symmetry properties to higher-order modes injected in the OPO. The physical situation is illustrated in Fig. 1. A pump beam is sent to the OPO cavity along with a seed beam

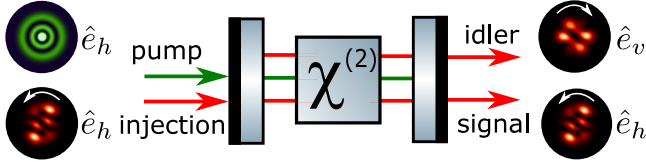


FIG. 1. Sketch of the optical parametric oscillator with type-II phase matching and structured light injection. \hat{e}_h and \hat{e}_v are the horizontal and vertical polarization unit vectors, respectively. The pump beam can be radially structured to optimize the spatial overlap with signal and idler.

that matches the signal frequency and polarization. Inside the resonator, the pump energy is transferred to signal and idler, which, under type-II phase matching, is generated with its polarization orthogonal to the signal beam.

The seed beam is assumed to be structured with an arbitrary superposition of Laguerre-Gaussian (LG) modes of the same order N_s , while the pump beam is assumed to be in a single LG mode without OAM. In the LG basis, the pump and seed electric fields can be written as

$$\begin{aligned}\mathcal{E}_{p_{\text{in}}}(\mathbf{r}) &= \alpha_{p_{\text{in}}} \psi^{0q_p}(\mathbf{r}), \\ \mathcal{E}_{s_{\text{in}}}(\mathbf{r}) &= \sum_l \alpha_{s_{\text{in}}}^{lq_s} \psi^{lq_s}(\mathbf{r}),\end{aligned}\quad (1)$$

where $\psi^{lq}(\mathbf{r})$ is a LG mode function with topological charge (OAM) l and radial index q , $\alpha_{s_{\text{in}}}^{lq}$ is the corresponding complex amplitude of the signal mode, and $\alpha_{p_{\text{in}}}$ is the pump complex amplitude. The mathematical expression of the LG modes in terms of the polar coordinates (r, ϕ) in the focal plane ($z = 0$) is given by [42]

$$\psi^{lq}(\mathbf{r}) = \sqrt{\frac{(2/\pi)^p p!}{(p+|l|)!}} \frac{(\sqrt{2}r)^{|l|}}{w^{|l|+1}} L_p^{|l|} \left(\frac{2r^2}{w^2} \right) e^{-\frac{r^2}{w^2}} e^{il\phi}, \quad (2)$$

where w is the beam radius and $L_p^{|l|}(\frac{2r^2}{w^2})$ is the generalized Laguerre polynomial.

The summation over the seed modes is constrained by $2q_s + |l| = N_s$. The choice of a fixed order for the seed beam is of experimental relevance since in this case all components evolve with the same Gouy phase and can be simultaneously mode matched to the OPO cavity.

A. Dynamical equations

These input modes feed the dynamics that governs the buildup of the intracavity fields. They constitute the source terms of the dynamical equations for the intracavity amplitudes. Let the intracavity electric fields in the LG basis be written as

$$\begin{aligned}\mathcal{E}_p(\mathbf{r}) &= \alpha_p \psi^{0q_p}(\mathbf{r}), \\ \mathcal{E}_j(\mathbf{r}) &= \sum_l \alpha_j^{lq_j} \psi^{lq_j}(\mathbf{r}),\end{aligned}\quad (3)$$

where the indices $j = s, i$ refer to signal and idler, respectively. The stimulated idler beam will populate the Laguerre-Gaussian modes with optimal overlap

$$\Lambda_{q_s q_i}^l = \int [\psi^{0q_p}(\mathbf{r})]^* \psi^{lq_s}(\mathbf{r}) \psi^{-lq_i}(\mathbf{r}) d^2\mathbf{r}, \quad (4)$$

with the pump and seed modes. This imposes OAM conservation $l_s + l_i = l_p$ and restricts the radial indices as well. Since the pump beam is assumed to carry zero OAM, the coupled signal and idler modes must have opposite topological charges. However, the radial mode selection for the idler beam is not so simple. It is determined by the maximum overlap with the pump and seed modes. This point will be clarified in our numerical examples.

Assuming the perfect resonance of the three fields, the dynamical equations for the intracavity mode amplitudes are

$$\begin{aligned}\frac{d\alpha_p}{dt} &= -\gamma_p \alpha_p + i\chi \sum_l \Lambda_{q_s q_i}^l \alpha_s^{lq_s} \alpha_i^{-lq_i} + \eta_p \alpha_{p_{\text{in}}}, \\ \frac{d\alpha_s^{lq_s}}{dt} &= -\gamma \alpha_s^{lq_s} + i\chi \Lambda_{q_s q_i}^{l*} \alpha_p (\alpha_i^{-lq_i})^* + \eta \alpha_{s_{\text{in}}}^{lq_s}, \\ \frac{d\alpha_i^{lq_i}}{dt} &= -\gamma \alpha_i^{lq_i} + i\chi \Lambda_{q_s q_i}^{l*} \alpha_p (\alpha_s^{-lq_s})^*,\end{aligned}\quad (5)$$

where χ is the nonlinear coupling constant, γ_p is the pump decay rate, γ is the common decay rate of signal and idler, η_p and η are the pump and signal input transmissions, respectively. We recall that the mode indices l and q_s run over the allowed values compatible with the seed order $N_s = 2q_s + |l|$, while the stimulated idler beam will carry the Laguerre-Gaussian modes with optimal overlap with the pump and seed modes.

Our analysis is significantly simplified when we define the normalized variables

$$\begin{aligned}\beta_p &= \chi \alpha_p / \gamma, & \beta_{p_{\text{in}}} &= \chi \eta_p \alpha_{p_{\text{in}}} / \gamma^2, \\ \beta_s^{lq_s} &= \chi \alpha_s^{lq_s} / \gamma, & \beta_{s_{\text{in}}}^{lq_s} &= \chi \eta \alpha_{s_{\text{in}}}^{lq_s} / \gamma^2, \\ \beta_i^{lq_i} &= \chi \alpha_i^{lq_i} / \gamma.\end{aligned}\quad (6)$$

With the normalized variables, the dynamical equations become

$$\begin{aligned}\dot{\beta}_p &= -\gamma_r \beta_p + i \sum_l \Lambda_{q_s q_i}^l \beta_s^{lq_s} \beta_i^{-lq_i} + \beta_{p_{\text{in}}}, \\ \dot{\beta}_s^{lq_s} &= -\beta_s^{lq_s} + i \Lambda_{q_s q_i}^{l*} \beta_p (\beta_i^{-lq_i})^* + \beta_{s_{\text{in}}}^{lq_s}, \\ \dot{\beta}_i^{lq_i} &= -\beta_i^{lq_i} + i \Lambda_{q_s q_i}^{l*} \beta_p (\beta_s^{-lq_s})^*,\end{aligned}\quad (7)$$

where dotted variables in the left-hand side are derivatives with respect to the dimensionless time $\tau = \gamma t$, and $\gamma_r = \gamma_p / \gamma$ is the decay ratio.

B. Steady-state solution

The output field distribution is given by the steady-state solution of the dynamical equations (7), which can be obtained by setting the time derivatives equal to zero in the left-hand side ($\dot{\beta}_p = \dot{\beta}_s^{lq_s} = \dot{\beta}_i^{lq_i} = 0$) and solving the resulting algebraic equations. From the last two equations we get

$$\begin{aligned}\beta_s^{lq_s} &= \frac{\beta_{s_{\text{in}}}^{lq_s}}{1 - |\Lambda_{q_s q_i}^l \beta_p|^2}, \\ \beta_i^{lq_i} &= \frac{i \beta_p \Lambda_{q_s q_i}^{l*} (\beta_{s_{\text{in}}}^{-lq_s})^*}{1 - |\Lambda_{q_s q_i}^l \beta_p|^2}.\end{aligned}\quad (8)$$

These equations can be plugged into the steady-state condition for the intracavity pump amplitude, resulting in

$$\left[\gamma_r + \sum_l \frac{|\Lambda_{q_s q_i}^l \beta_{s_{in}}^{l q_s}|^2}{(1 - |\Lambda_{q_s q_i}^l \beta_p|^2)^2} \right] \beta_p = \beta_{p_{in}}, \quad (9)$$

where we used $\Lambda_{q_s q_i}^{-l} = \Lambda_{q_s q_i}^l$. Without loss of generality, we may set the input pump phase equal to zero ($\alpha_{p_{in}} \in \mathbb{R}$). Therefore, the intracavity pump amplitude is also a real number that can be found by solving the quintic equation (9). For arbitrary mode orders, this is usually a difficult task that is beyond the scope of this work. Nevertheless, Eq. (8) allow us to establish an interesting property of the down-converted beams generated by the nonlinear process, without the need of the intracavity pump solution. As we discuss next, the relationship between the amplitudes of the seed beam and the intracavity down-converted fields sets an interesting symmetry relation between signal and idler in a generalized Poincaré sphere representation of higher-order modes.

III. GENERALIZED POINCARÉ SYMMETRY

The Poincaré sphere representation of OAM beams has been first introduced for first-order modes [32]. It describes linear combinations of Laguerre-Gaussian modes with radial number $q = 0$ and topological charges $l = \pm 1$. In our case, we will use an independent Poincaré sphere for each two-dimensional mode space spanned by Laguerre-Gaussian beams with opposite OAM, $\psi^{\pm l q}$. For the signal beam, l and q_s run over the allowed values compatible with $2q_s + |l| = N$. For the idler beam, the radial numbers are defined by those modes with maximal spatial overlap with the pump and seed modes. Note that a zero OAM component $l = 0$ can only occur in even orders for $q_s = N/2$, while the LG modes with odd orders have $l \neq 0$. In this way, we can group the LG modes of a given order in pairs with opposite OAM $\{\psi^{\pm l q}\}$ and an isolated mode with zero OAM for even orders. For example, for seed beams with orders from 0 to 4 we have

$$\begin{aligned} N = 0: & \quad \{\psi^{00}\}, \\ N = 1: & \quad \{\psi^{\pm 10}\}, \\ N = 2: & \quad \{\psi^{\pm 20}\} \oplus \{\psi^{01}\}, \\ N = 3: & \quad \{\psi^{\pm 30}\} \oplus \{\psi^{\pm 11}\}, \\ N = 4: & \quad \{\psi^{\pm 40}\} \oplus \{\psi^{\pm 21}\} \oplus \{\psi^{02}\}. \end{aligned} \quad (10)$$

Note that each $\{\psi^{\pm l q_s}\}$ subspace realizes an independent SU(2) structure.

The idler modes will follow a similar structure. However, the corresponding radial numbers are selected by the optimal overlap with the pump and seed modes and, in general, do not fix a given order. As we will see, the Poincaré sphere symmetry previously demonstrated for first-order modes in Refs. [33,34] is independently verified within each one of the two-dimensional OAM subspaces for higher orders.

From Eq. (8) we can see that the intracavity signal and idler amplitudes are related by

$$\beta_i^{l q_i} = i \beta_p \Lambda_{q_s q_i}^{l*} (\beta_s^{-l q_s})^*. \quad (11)$$

For $l = 0$, there is no SU(2) structure and this equation simply states the conjugate relation between signal and idler amplitudes for the zero OAM modes. In this case, no Poincaré symmetry can be realized. However, when $l \neq 0$, Eq. (11) sets a connection between the SU(2) structures of signal and idler. Let the signal input be an arbitrary structure of order $N = 2q_s + |l|$, which can be written as

$$\mathcal{E}_{s_{in}} = \sum_{l>0} A_{in}^{l q_s} [\cos(\theta_l/2) \psi^{l q_s} + e^{i\phi_l} \sin(\theta_l/2) \psi^{-l q_s}], \quad (12)$$

where $\{A_{in}^{l q}\}$ are complex amplitudes and $\{(\theta_l, \phi_l)\}$ are the Poincaré sphere coordinates that represent the seed mode in each SU(2) structure $\mathcal{H}^l \equiv \{\psi^{\pm l q}\}$. For a given order N , a Poincaré sphere is associated with each OAM value l . With these definitions, the source terms that figure in the dynamical equations (7) become

$$\begin{aligned} \beta_{s_{in}}^{l q_s} &= \frac{\chi \eta}{\gamma^2} A_{in}^{l q_s} \cos(\theta_l/2), \\ \beta_{s_{in}}^{-l q_s} &= \frac{\chi \eta}{\gamma^2} A_{in}^{l q_s} e^{i\phi_l} \sin(\theta_l/2). \end{aligned} \quad (13)$$

From the steady-state solution (8) and the signal-idler conjugation relation (11), we easily get

$$\begin{aligned} \beta_s^{l q_s} &= \frac{\chi}{\gamma} \xi_s^{l q_s} \cos(\theta_l/2), \quad \beta_s^{-l q_s} = \frac{\chi}{\gamma} \xi_s^{l q_s} e^{i\phi_l} \sin(\theta_l/2), \\ \beta_i^{l q_i} &= \frac{\chi}{\gamma} \xi_i^{l q_i} e^{-i\phi_l} \sin(\theta_l/2), \quad \beta_i^{-l q_i} = \frac{\chi}{\gamma} \xi_i^{l q_i} \cos(\theta_l/2), \end{aligned} \quad (14)$$

where

$$\begin{aligned} \xi_s^{l q_s} &= \frac{\eta A_{in}^{l q_s} / \gamma}{1 - |\Lambda_{q_s q_i}^l \beta_p|^2}, \\ \xi_i^{l q_i} &= i \beta_p \Lambda_{q_s q_i}^{l*} (\xi_s^{l q_s})^*. \end{aligned} \quad (15)$$

Equations (14) set the Poincaré sphere symmetry between signal and idler spatial modes. Indeed, we can easily see that signal and idler coordinates on the sphere are related by

$$\begin{aligned} \theta_i^i &= \pi - \theta_l^s, \\ \phi_l^i &= \phi_l^s, \end{aligned} \quad (16)$$

which means that within each SU(2) structure \mathcal{H}^l , signal and idler are represented by two points on the sphere that are the specular image of each other with respect to the equatorial plane. This is a generalization of the first-order mode symmetry previously demonstrated in Refs. [33,34]. The intracavity signal and idler spatial modes are then given by

$$\begin{aligned} \mathcal{E}_s &= \sum_{l>0} \xi_s^{l q_s} [\cos(\theta_l/2) \psi^{l q_s} + e^{i\phi_l} \sin(\theta_l/2) \psi^{-l q_s}], \\ \mathcal{E}_i &= \sum_{l>0} \xi_i^{l q_i} [e^{-i\phi_l} \sin(\theta_l/2) \psi^{l q_i} + \cos(\theta_l/2) \psi^{-l q_i}]. \end{aligned} \quad (17)$$

We next discuss some examples which allow us to visualize the generalization of the Poincaré sphere symmetry between signal and idler spatial modes. As we will see, the odd modes already capture the essential features of the symmetry since for even orders the zero OAM components do not possess the required SU(2) structure.

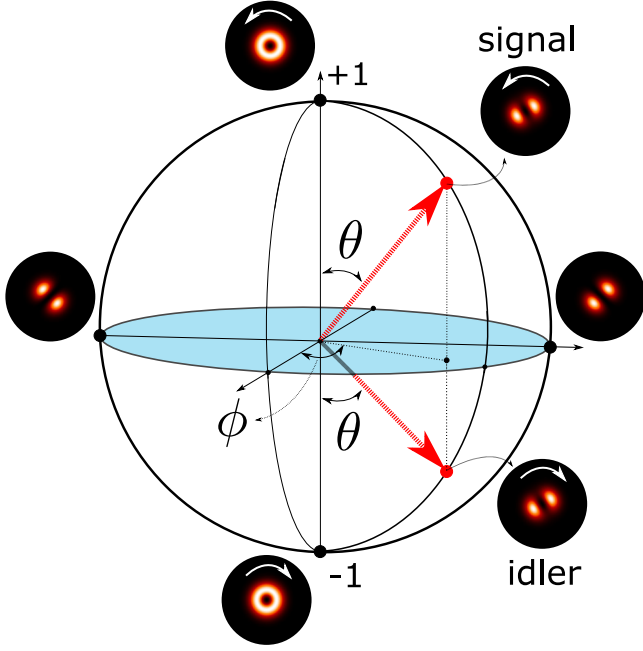


FIG. 2. Poincaré sphere representation for first-order OAM symmetry.

A. First order revisited

We now briefly revisit the first-order case already discussed in Refs. [33,34]. In this case, we can assume a Gaussian pump ($q_p = 0$) and a first-order signal input,

$$\begin{aligned} \mathcal{E}_{p_{in}} &= \alpha_{p_{in}} \psi^{00}, \\ \mathcal{E}_{s_{in}} &= A_{in}^{10} [\cos(\theta/2) \psi^{10} + e^{i\phi} \sin(\theta/2) \psi^{-10}]. \end{aligned} \quad (18)$$

The steady-state intracavity pump amplitude is given by the solution of the quintic equation

$$\left[\gamma_r + \frac{|\Lambda_{00}^1 A_{in}^{10}|^2}{(1 - |\Lambda_{00}^1 \beta_p|^2)^2} \right] \beta_p = \beta_{p_{in}}. \quad (19)$$

Then, the intracavity signal and idler spatial structures are

$$\begin{aligned} \mathcal{E}_s &= \xi_s^{10} [\cos(\theta/2) \psi^{10} + e^{i\phi} \sin(\theta/2) \psi^{-10}], \\ \mathcal{E}_i &= \xi_i^{10} [e^{-i\phi} \sin(\theta/2) \psi^{10} + \cos(\theta/2) \psi^{-10}], \end{aligned} \quad (20)$$

with the mode amplitudes given by

$$\begin{aligned} \xi_s^{10} &= \frac{\eta A_{in}^{10} / \gamma}{1 - |\Lambda_{00}^1 \beta_p|^2}, \\ \xi_i^{10} &= i \beta_p \Lambda_{00}^{1*} (\xi_s^{10})^*. \end{aligned} \quad (21)$$

The coordinates of the points representing the signal and idler structures in the Poincaré sphere are related by

$$\begin{aligned} \theta^i &= \pi - \theta^s, \\ \phi^i &= \phi^s. \end{aligned} \quad (22)$$

As shown in Fig. 2, the point representing the idler mode is the specular image of the point representing the signal with respect to the equatorial plane. This symmetry provides optimal intensity overlap and OAM conservation between signal and idler.

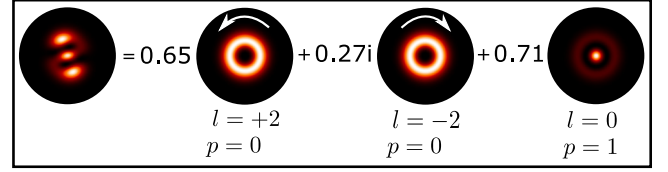


FIG. 3. Example of a second-order seed beam. In this case we have set $A_{in}^{01} = A_{in}^{20} = 1/\sqrt{2}$, $\theta = 45^\circ$, and $\phi = 90^\circ$.

B. Poincaré symmetry with a second-order seed

The even-order subspaces include a zero-OAM mode with radial number $q = N/2$. Since it is an isolated single-mode subspace, there is no room for a Poincaré sphere representation or symmetry relation. The remaining OAM carrying modes can be grouped in pairs with opposite OAM, constituting a set of independent SU(2) structures where the aforementioned symmetry is verified. For example, consider the case of a second-order seed beam $\{\psi^{\pm 20}, \psi^{01}\}$ and a single-mode pump with zero OAM and radial order $q_p = 1$,

$$\begin{aligned} \mathcal{E}_{p_{in}} &= \alpha_{p_{in}} \psi^{01}, \\ \mathcal{E}_{s_{in}} &= A_{in}^{01} \psi^{01} + A_{in}^{20} [\cos(\theta/2) \psi^{20} + e^{i\phi} \sin(\theta/2) \psi^{-20}]. \end{aligned} \quad (23)$$

An example of one such structure is shown in Fig. 3. The idler modes which will profit from the pump and seed energy are those with maximum spatial overlap with the input modes. First, OAM conservation is required for nonvanishing overlap. Then, the radial order associated with each OAM is determined by the maximum numerical value of the overlap integrals $\Lambda_{0q_i}^2$ and $\Lambda_{1q_i}^0$. In Fig. 4 we show the numerical value of the overlap integrals as a function of the idler radial order.

As we can see, for both $l = 0$ and ± 2 , the zero radial order ($q_i = 0$) displays optimal coupling. Therefore, the transverse modes taking part in the intracavity interaction are $\{\psi^{01}\}$ for the pump, $\{\psi^{01}, \psi^{\pm 20}\}$ for the signal, and $\{\psi^{00}, \psi^{\pm 20}\}$ for the idler. In this case, the pump steady state is given by the solution of

$$\left[\gamma_r + \frac{|\Lambda_{10}^0 A_{in}^{01}|^2}{(1 - |\Lambda_{10}^0 \beta_p|^2)^2} + \frac{|\Lambda_{00}^2 A_{in}^{20}|^2}{(1 - |\Lambda_{00}^2 \beta_p|^2)^2} \right] \beta_p = \beta_{p_{in}}, \quad (24)$$

and the steady-state amplitudes of signal and idler are

$$\begin{aligned} \mathcal{E}_s &= \xi_s^{01} \psi^{01} + \xi_s^{20} [\cos(\theta/2) \psi^{20} + e^{i\phi} \sin(\theta/2) \psi^{-20}], \\ \mathcal{E}_i &= \xi_i^{00} \psi^{00} + \xi_i^{20} [e^{-i\phi} \sin(\theta/2) \psi^{20} + \cos(\theta/2) \psi^{-20}], \end{aligned} \quad (25)$$

with the mode amplitudes given by

$$\begin{aligned} \xi_s^{01} &= \frac{\eta A_{in}^{01} / \gamma}{1 - |\Lambda_{10}^0 \beta_p|^2}, & \xi_s^{20} &= \frac{\eta A_{in}^{20} / \gamma}{1 - |\Lambda_{00}^2 \beta_p|^2}, \\ \xi_i^{00} &= i \beta_p \Lambda_{10}^{0*} (\xi_s^{01})^*, & \xi_i^{20} &= i \beta_p \Lambda_{00}^{2*} (\xi_s^{20})^*. \end{aligned} \quad (26)$$

Note that no special symmetry can be realized in the zero OAM subspace, only the usual conjugation relation between signal and idler amplitudes. However, as shown in Fig. 5, the $l = \pm 2$ subspace displays the same kind of Poincaré sphere symmetry as the first-order case, with the signal and idler

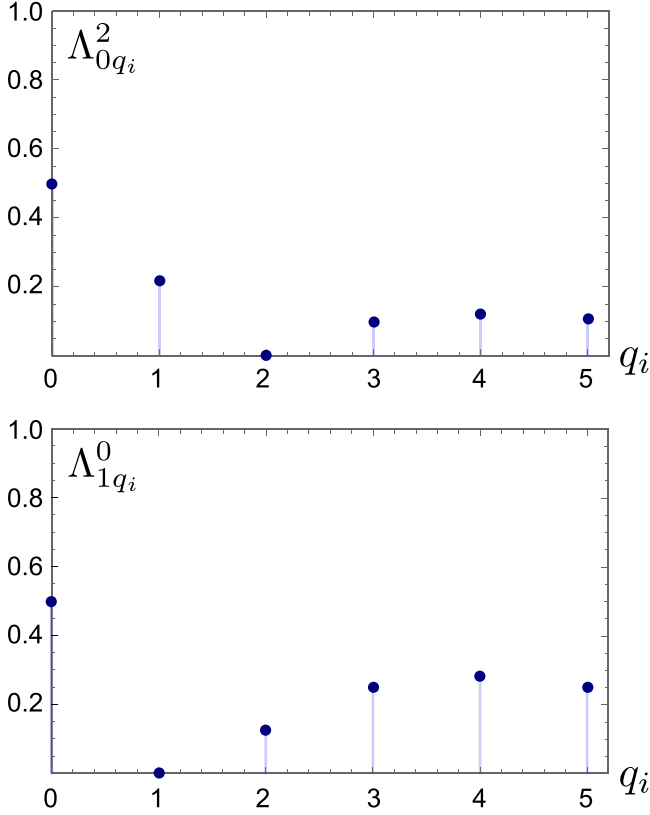


FIG. 4. Pump-signal-idler overlap integrals for $l = \pm 2$ (top) and $l = 0$ (bottom) as a function of the idler radial orders, when the pump parameters are fixed at $l_p = 0$ and $q_p = 1$.

coordinates related by

$$\begin{aligned}\theta^i &= \pi - \theta^s, \\ \phi^i &= \phi^s.\end{aligned}\quad (27)$$

C. Two-sphere symmetry for third-order beams

The simplest case with more than one Poincaré sphere symmetry is realized by a third-order seed beam. As before, the pump is assumed to carry zero OAM and optimal overlap is attained with $q_p = 2$. In Fig. 6 we show the overlap integrals for different OAM values. As we can see, the largest coupling between signal and idler modes with $l = \pm 1$ and ± 3 occurs for the idler radial index $q_i = 0$. Therefore, the $l = \pm 3$ sphere represents signal and idler modes with $q_s = q_i = 0$. However, the $l = \pm 1$ sphere represents signal modes with $q_s = 1$ and idler modes with $q_i = 0$. In any case, the radial numbers are irrelevant for the Poincaré symmetry condition, which is essentially determined by OAM conservation.

With these input modes, the source terms in the dynamical equations become

$$\begin{aligned}\mathcal{E}_{p_{in}} &= \alpha_{p_{in}} \psi^{02}, \\ \mathcal{E}_{s_{in}} &= A_{in}^{30} [\cos(\theta_3/2) \psi^{30} + e^{i\phi_3} \sin(\theta_3/2) \psi^{-30}] \\ &\quad + A_{in}^{11} [\cos(\theta_1/2) \psi^{11} + e^{i\phi_1} \sin(\theta_1/2) \psi^{-11}].\end{aligned}\quad (28)$$

Two sets of Poincaré sphere coordinates are used, (θ_1, ϕ_1) and (θ_3, ϕ_3) , associated with the $l = \pm 1$ and ± 3 manifolds,

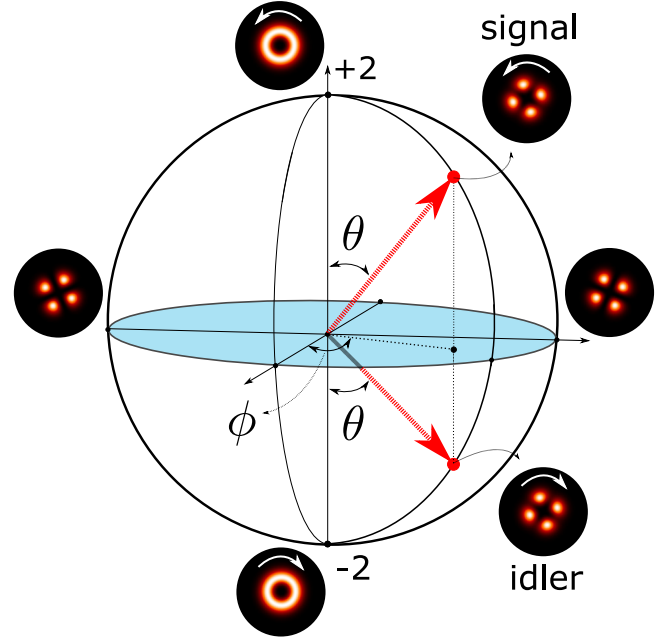


FIG. 5. Signal and idler symmetry in the Poincaré sphere for second-order OAM ($l = \pm 2$).

respectively. In Fig. 7 we show an example of seed beam and its decomposition in these manifolds.

The steady-state intracavity pump amplitude is given by the solution of the quintic equation

$$\left[\gamma_r + \frac{|\Lambda_{00}^3 A_{in}^{30}|^2}{(1 - |\Lambda_{00}^3 \beta_p|^2)^2} + \frac{|\Lambda_{10}^1 A_{in}^{11}|^2}{(1 - |\Lambda_{10}^1 \beta_p|^2)^2} \right] \beta_p = \beta_{p_{in}}.\quad (29)$$

Once the solution of Eq. (29) is obtained, the intracavity signal and idler spatial structures can be readily calculated from

$$\begin{aligned}\mathcal{E}_s &= \xi_s^{30} [\cos(\theta_3/2) \psi^{30} + e^{i\phi_3} \sin(\theta_3/2) \psi^{-30}] \\ &\quad + \xi_s^{11} [\cos(\theta_1/2) \psi^{11} + e^{i\phi_1} \sin(\theta_1/2) \psi^{-11}], \\ \mathcal{E}_i &= \xi_i^{30} [e^{-i\phi_3} \sin(\theta_3/2) \psi^{30} + \cos(\theta_3/2) \psi^{-30}] \\ &\quad + \xi_i^{10} [e^{-i\phi_1} \sin(\theta_1/2) \psi^{10} + \cos(\theta_1/2) \psi^{-10}],\end{aligned}\quad (30)$$

with the mode amplitudes given by

$$\begin{aligned}\xi_s^{30} &= \frac{\eta A_{in}^{30} / \gamma}{1 - |\Lambda_{00}^3 \beta_p|^2}, & \xi_s^{11} &= \frac{\eta A_{in}^{11} / \gamma}{1 - |\Lambda_{10}^1 \beta_p|^2}, \\ \xi_i^{30} &= i \beta_p \Lambda_{00}^{3*} (\xi_s^{30})^*, & \xi_i^{10} &= i \beta_p \Lambda_{10}^{1*} (\xi_s^{11})^*.\end{aligned}\quad (31)$$

These mode superpositions are represented in the Poincaré spheres shown in Fig. 8. The signal and idler coordinates are related by

$$\begin{aligned}\theta_3^i &= \pi - \theta_3^s, & \phi_3^i &= \phi_3^s, \\ \theta_1^i &= \pi - \theta_1^s, & \phi_1^i &= \phi_1^s.\end{aligned}\quad (32)$$

These relations show that the signal and idler modes verify the Poincaré symmetry independently on each sphere. We have also tested the symmetry condition with a numerical integration of the dynamical equations. The numerical results for the signal and idler mode amplitudes are displayed in

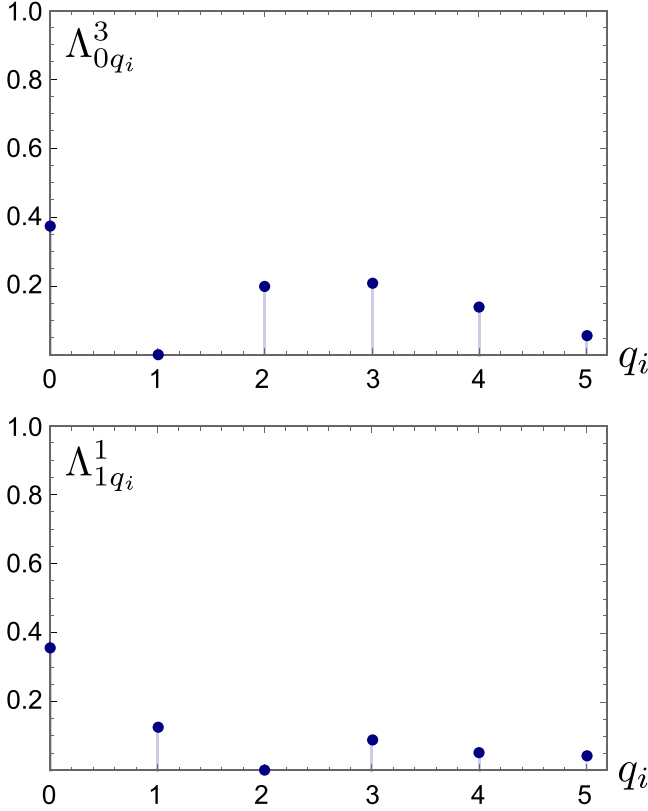


FIG. 6. Pump-signal-idler spatial overlap for $l = \pm 3$ (top) and $l = \pm 1$ (bottom) as a function of the idler radial orders, when the pump parameters are fixed at $l_p = 0$ and $q_p = 2$.

Fig. 9, along with the resulting two-sphere representation. The spherical coordinates are evaluated from the numerical results, confirming the two-sphere symmetry condition.

As before, this condition ensures both maximal intensity overlap and OAM conservation. The extension of this symmetry condition to higher orders is straightforward. The mode space can be split in two-dimensional OAM subspaces with fixed absolute value $|l| = 1, 2, 3, \dots$, where the symmetry condition is simultaneously verified on independent Poincaré spheres. For even orders, there is an isolated component with zero OAM, where no symmetry condition can be realized other than the usual phase conjugation between signal and idler amplitudes.

IV. OAM-STRUCTURED PUMP

It is also interesting to investigate how the Poincaré sphere symmetry between signal and idler is affected by a pump

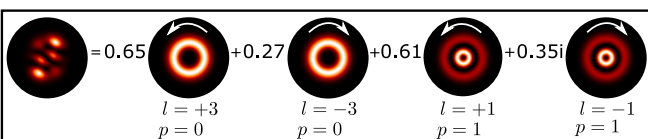


FIG. 7. Example of a third-order seed beam with $A_{in}^{11} = A_{in}^{30} = 1/\sqrt{2}$. The coordinates on the Poincaré spheres for $l = \pm 3$ and ± 1 are $(\theta_3 = 45^\circ, \phi_3 = 0^\circ)$ and $(\theta_1 = 60^\circ, \phi_1 = 90^\circ)$, respectively.

beam carrying OAM. In this case, a Poincaré representation also applies to the pump beam. For example, let us consider a pump beam prepared in a superposition of second-order modes with $l = \pm 2$ and $q_p = 0$. The seed beam is assumed to be a first-order superposition of modes with $l = \pm 1$. The pump and seed input amplitudes can be written as

$$\begin{aligned} \mathcal{E}_{p_{in}} &= A_{p_{in}} [\cos(\theta_p/2) \psi^{20} + e^{i\phi_p} \sin(\theta_p/2) \psi^{-20}], \\ \mathcal{E}_{s_{in}} &= A_{s_{in}} [\cos(\theta_s/2) \psi^{10} + e^{i\phi_s} \sin(\theta_s/2) \psi^{-10}], \end{aligned} \quad (33)$$

where (θ_p, ϕ_p) and (θ_s, ϕ_s) are the Poincaré sphere coordinates of the input pump and seed beams, respectively. In Fig. 10, we display the Poincaré representation of the pump (left) and seed (right) input modes. The idler modes with optimal intensity overlap and OAM conservation with the seed are also first-order LG modes with $l = \pm 1$ and $q_i = 0$.

The time evolution of the pump, signal, and idler intracavity amplitudes is governed by the following dynamical equations:

$$\begin{aligned} \dot{\beta}_p^+ &= -\gamma_r \beta_p^+ + i\Lambda \beta_s^+ \beta_i^+ + \beta_{p_{in}} \cos(\theta_p/2), \\ \dot{\beta}_p^- &= -\gamma_r \beta_p^- + i\Lambda \beta_s^- \beta_i^- + \beta_{p_{in}} e^{i\phi_p} \sin(\theta_p/2), \\ \dot{\beta}_s^+ &= -\beta_s^+ + i\Lambda^* \beta_p^+ \beta_i^{+*} + \beta_{s_{in}} \cos(\theta_s/2), \\ \dot{\beta}_s^- &= -\beta_s^- + i\Lambda^* \beta_p^- \beta_i^{-*} + \beta_{s_{in}} e^{i\phi_s} \sin(\theta_s/2), \\ \dot{\beta}_i^\pm &= -\beta_i^\pm + i\Lambda^* \beta_p^\pm (\beta_s^\pm)^*, \end{aligned} \quad (34)$$

where β_p^\pm are the normalized pump amplitudes for $l = \pm 2$, $\beta_{s(i)}^\pm$ are the normalized seed (idler) amplitudes for $l = \pm 1$, and the time derivatives in the left-hand side are taken with respect to the dimensionless parameter $\tau = \gamma t$. The mode coupling is mediated by the three-mode overlap

$$\Lambda = \int [\psi_p^{\pm 20}(\mathbf{r})]^* \psi_s^{\pm 10}(\mathbf{r}) \psi_i^{\pm 10}(\mathbf{r}) d^2\mathbf{r}. \quad (35)$$

The steady-state solutions are obtained by setting the time derivatives equal to zero in the left-hand side of Eqs. (34) and solving the resulting algebraic equations. From the last three equations in (34), we have

$$\begin{aligned} \beta_s^+ &= \xi_s^+ \cos(\theta_s/2), & \beta_s^- &= \xi_s^- e^{i\phi_s} \sin(\theta_s/2), \\ \beta_i^+ &= \xi_i^+ \cos(\theta_s/2), & \beta_i^- &= \xi_i^- e^{-i\phi_s} \sin(\theta_s/2), \end{aligned} \quad (36)$$

where we defined

$$\begin{aligned} \xi_s^\pm &= \frac{\eta A_{s_{in}}/\gamma}{1 - |\Lambda \beta_p^\pm|^2}, \\ \xi_i^\pm &= i\beta_p^\pm \Lambda^* (\xi_s^\pm)^*. \end{aligned} \quad (37)$$

The steady-state intracavity pump amplitudes are given by the solutions of two independent quintic equations

$$\begin{aligned} \left[\gamma_r + \frac{|\Lambda A_{s_{in}}|^2 \cos^2(\frac{\theta_s}{2})}{(1 - |\Lambda \beta_p^+|^2)^2} \right] \beta_p^+ &= \beta_{p_{in}} \cos\left(\frac{\theta_p}{2}\right), \\ \left[\gamma_r + \frac{|\Lambda A_{s_{in}}|^2 \sin^2(\frac{\theta_s}{2})}{(1 - |\Lambda \beta_p^-|^2)^2} \right] \beta_p^- &= \beta_{p_{in}} e^{i\phi_p} \sin\left(\frac{\theta_p}{2}\right). \end{aligned} \quad (38)$$

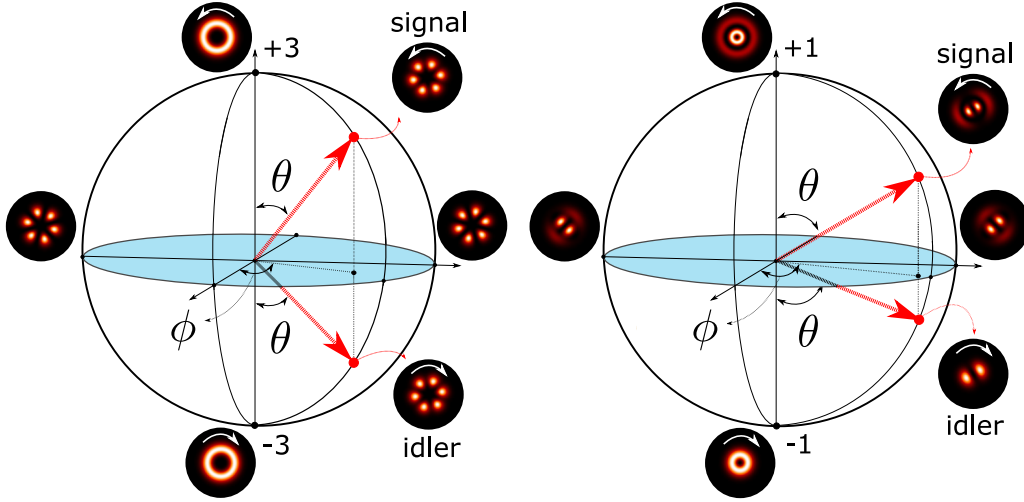


FIG. 8. Third-order OAM symmetry. On left side we can visualize the symmetry relation verified in the Poincaré sphere for $l = \pm 3$ and on the right side the same symmetry is displayed on the independent sphere for $l = \pm 1$.

From Eqs. (36) we immediately obtain the complete structure of the intracavity signal and idler fields as

$$\begin{aligned} \mathcal{E}_s &= \xi_s^+ \cos(\theta_s/2) \psi_s^{+10} + \xi_s^- e^{i\phi_s} \sin(\theta_s/2) \psi_s^{-10}, \\ \mathcal{E}_i &= \xi_i^+ \cos(\theta_s/2) \psi_i^{+10} + \xi_i^- e^{-i\phi_s} \sin(\theta_s/2) \psi_i^{-10}. \end{aligned} \quad (39)$$

The Poincaré sphere representation of signal and idler depends on both the seed and pump parameters. While the seed parameters are explicit in the expressions above, the dependence on the pump is implicit through $\xi_{s,i}^\pm$.

Assuming weak pump and seed powers, the pump is not significantly depleted by the parametric interaction and the intracavity pump is essentially driven by the external input,

leading to

$$\begin{aligned} \beta_p^+ &\approx \frac{\beta_{p_{in}}}{\gamma_r} \cos(\theta_p/2), \\ \beta_p^- &\approx \frac{\beta_{p_{in}}}{\gamma_r} e^{i\phi_p} \sin(\theta_p/2). \end{aligned} \quad (40)$$

In this case, we can write the analytical solutions for signal and idler as

$$\mathcal{E}_s = \xi_s^+ \cos\left(\frac{\theta_s}{2}\right) \psi^{+10} + \xi_s^- e^{i\phi_s} \sin\left(\frac{\theta_s}{2}\right) \psi^{-10}, \quad (41)$$

$$\begin{aligned} \mathcal{E}_i &= \xi_i^+ \cos\left(\frac{\theta_s}{2}\right) \cos\left(\frac{\theta_p}{2}\right) \psi^{+10} \\ &+ \xi_i^- e^{i(\phi_p - \phi_s)} \sin\left(\frac{\theta_s}{2}\right) \sin\left(\frac{\theta_p}{2}\right) \psi^{-10}, \end{aligned} \quad (42)$$

where the amplitudes can be explicitly written in terms of the pump parameters as

$$\begin{aligned} \xi_s^\pm &= \frac{\eta A_{s_{in}}/\gamma}{1 - \frac{|\Lambda \beta_{p_{in}}|^2}{2\gamma_r^2} (1 \pm \cos \theta_p)}, \\ \xi_i^\pm &= i\beta_p^\pm \Lambda^* (\xi_s^\pm)^*. \end{aligned} \quad (43)$$

In this regime, the Poincaré symmetry becomes more evident for special values of the pump and seed parameters. First, for $\theta_p = \pi/2$ and arbitrary ϕ_p , we easily obtain that $\theta_i = \theta_s$ and $\phi_i = \phi_p - \phi_s$. This symmetry is displayed in Fig. 11 for $\phi_p = 0$. The idler spatial structure is represented by the specular image of the signal with respect to the great circle $\phi = 0$.

Moreover, restricting the input pump power to values well below the free-running oscillation threshold, such that

$$\frac{|\Lambda \beta_{p_{in}}|^2}{2\gamma_r^2} \ll 1, \quad (44)$$

one can take $\xi_s^+ \approx \xi_s^-$ and $\xi_i^+ \approx \xi_i^-$. From Eqs. (41) and (42), it is easy to see that the idler parameters are related to the

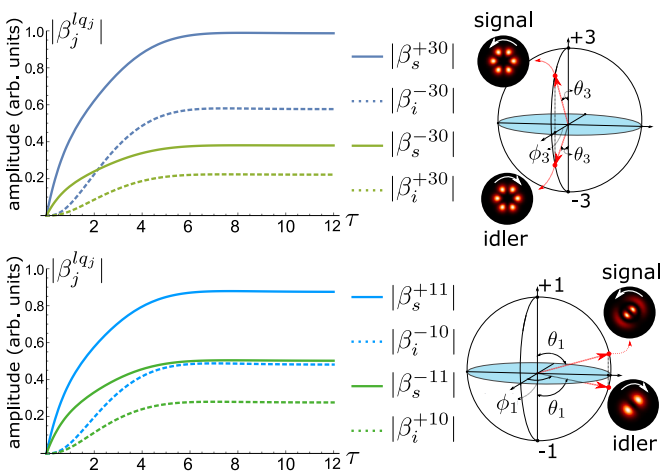
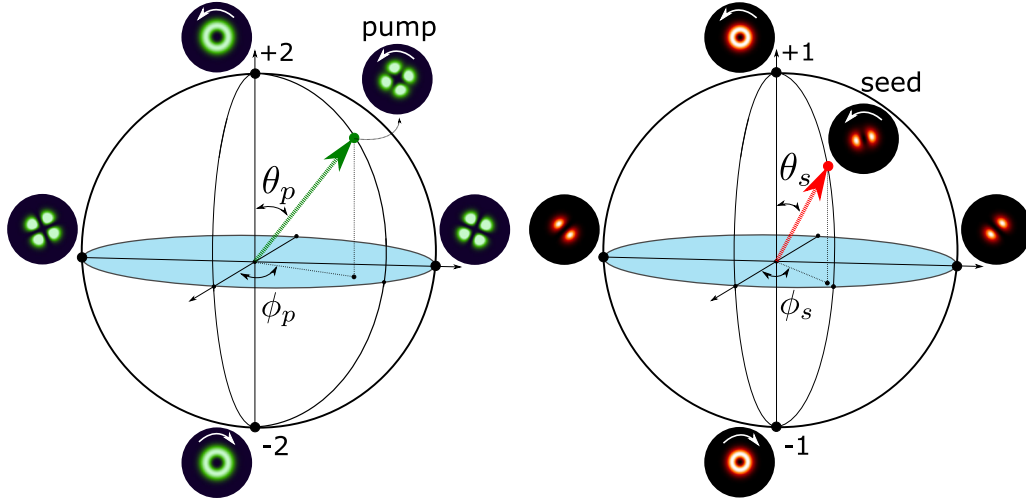


FIG. 9. Two-sphere symmetry for the numerical simulation of the OPO dynamics under third-order injection. The spherical coordinates for $l = \pm 3$ are $\theta_3 = 0.73$ rad and $\phi_3 = 0$. For $l = \pm 1$ the coordinates are $\theta_1 = 1.04$ rad and $\phi_1 = 1.57$ rad. The pump, seed, and decay parameters were set to $\beta_{p_{in}} = 2$, $A_{in}^{30} = A_{in}^{11} = 1/\sqrt{2}$, and $\gamma_r = 1$, respectively. The free-running oscillation threshold is $\beta_{p_{th}} \approx 2.7$.

FIG. 10. Poincaré sphere representations of the pump ($l = \pm 2$) and seed ($l = \pm 1$) beams.

pump and seed parameters as

$$\phi_i = \phi_p - \phi_s, \quad (45)$$

$$\tan\left(\frac{\theta_i}{2}\right) = \tan\left(\frac{\theta_p}{2}\right) \tan\left(\frac{\theta_s}{2}\right). \quad (46)$$

Therefore, the seed and idler beams are azimuthally symmetric in the first-order Poincaré sphere with respect to the angle $\phi_p/2$, while the idler polar location follows a nontrivial relation with the pump and seed polar parameters. Another interesting condition within this regime occurs for $\theta_s = \pi/2$ and $\phi_s = 0$. In this case, the idler parameters become equal to those of the pump, $\theta_i = \theta_p$ and $\phi_i = \phi_p$. Therefore, the idler spatial structure can be actively controlled by fixing either the

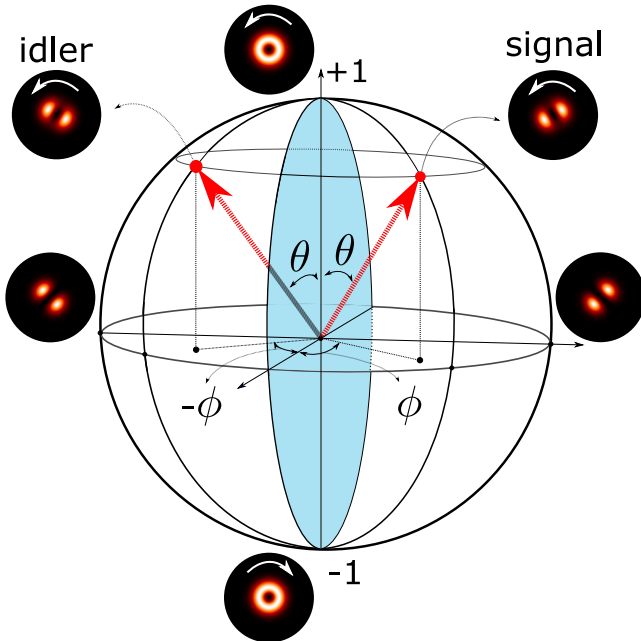
pump or the seed parameters and varying the others. In a real experimental situation, this active control can be challenged by the astigmatic effects caused by the crystal birefringence [28]. However, this effect can be compensated for with a two-crystal setup, as the one used in Refs. [38,39]. Active control of signal and idler spatial structures exploring symmetry conditions can be useful for shaping spatial quantum correlations generated in parametric amplification.

V. EXPERIMENTAL PROPOSAL

In this section, we propose an experimental setup to investigate the generalized OAM symmetry. In Fig. 12, we present the sketch of the proposed setup. We consider a dual-wavelength laser source that provides both the OPO pump at visible (VIS) wavelength and the injection seed at the infrared (IR). As we discussed, both wavelengths must be transverse structured in order to maximize the spatial overlap between pump, signal, and idler. This can be realized using spatial light modulators represented as the *mode preparation* boxes on the top of Fig. 12.

After the mode preparation stage, the structured pump and seed beams pass through mode-matching lenses and are sent to the OPO cavity. A quasiconcentric cavity configuration is convenient since some extra space is needed for astigmatism compensation with a half-wave plate (HWP) oriented at 45° , and a second crystal rotated by 90° with respect to the first one [38,39]. Note that this wave plate must introduce a π ($\lambda/2$) retardation at the down-converted wavelength and a 2π (λ) retardation at the pump. In this manner the polarization of the down-converted beam is rotated by 90° , while the pump polarization remains unchanged and the nonlinear process is restricted to the first crystal. Under type-II phase matching, we can separate the down-converted beams with a polarizing beam splitter (PBS).

The cavity Airy peaks can be monitored with photodiode detectors plugged to an oscilloscope, as the cavity length is scanned by a piezoelectric (PZT) ceramic attached to the output mirror and controlled by a function generator (FG). The triple resonance condition can be achieved by adjusting

FIG. 11. Poincaré sphere representation of the intracavity signal and idler structures when $\theta_p = \pi/2$ and $\phi_p = 0$.

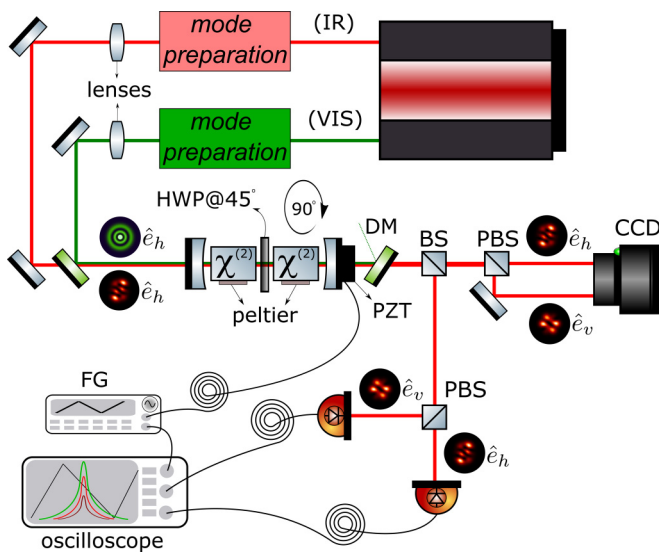


FIG. 12. Sketch of the proposed experimental setup to investigate the OAM symmetry. After the mode preparation stage, the pump and seed beams are mode matched to the OPO resonator. A two-crystal scheme with a half-wave plate (HWP) is proposed for astigmatism compensation. A dichroic mirror (DM) is used to filter out the pump beam at the OPO output. Under type-II phase matching, the down-converted beams can be separated with a polarizing beam splitter (PBS) and independently imaged with a charge-coupled device (CCD) camera.

the crystal's temperature with a peltier. The pump beam at visible wavelength can be filtered out of the OPO output with

a dichroic mirror (DM), leaving the down-converted beams on the path to intensity measurement and image acquisition.

VI. CONCLUSION

In conclusion, we derived a generalized Poincaré symmetry for optical parametric amplification of beams carrying orbital angular momentum. The first-order symmetry is extended to more complex mode structures involving the superposition of different OAM components. We show that the Poincaré symmetry is simultaneously verified in each independent OAM subspace, thus establishing a set of signal and idler modes independently related by the symmetry condition. Moreover, when the pump beam is structured with OAM modes, a different kind of Poincaré symmetry is obtained. In all cases, we have taken into account the numerical values of the overlap integrals that determine the intermode coupling strength and select the most adapted modes. These symmetry and coupling conditions can be important for establishing parallel channels for quantum information transmission, a potentially fruitful subject for future investigation.

ACKNOWLEDGMENTS

Funding was provided by Conselho Nacional de Desenvolvimento Científico e Tecnológico (CNPq), Coordenação de Aperfeiçoamento de Pessoal de Nível Superior (CAPES), Fundação Carlos Chagas Filho de Amparo à Pesquisa do Estado do Rio de Janeiro (FAPERJ), and Instituto Nacional de Ciência e Tecnologia de Informação Quântica (INCT-IQ Grant No. 465469/2014-0).

- [1] S. Reynaud, C. Fabre, and E. Giacobino, Quantum fluctuations in a two-mode parametric oscillator, *J. Opt. Soc. Am. B* **4**, 1520 (1987).
- [2] A. Heidmann, R. J. Horowicz, S. Reynaud, E. Giacobino, C. Fabre, and G. Camy, Observation of Quantum Noise Reduction on Twin Laser Beams, *Phys. Rev. Lett.* **59**, 2555 (1987).
- [3] J. Mertz, T. Debuisschert, A. Heidmann, C. Fabre, and E. Giacobino, Improvements in the observed intensity correlation of optical parametric oscillator twin beams, *Opt. Lett.* **16**, 1234 (1991).
- [4] Z. Y. Ou, S. F. Pereira, H. J. Kimble, and K. C. Peng, Realization of the Einstein-Podolsky-Rosen Paradox for Continuous Variables, *Phys. Rev. Lett.* **68**, 3663 (1992).
- [5] A. S. Villar, M. Martinelli, C. Fabre, and P. Nussenzveig, Direct Production of Tripartite Pump-Signal-Idler Entanglement in the Above-Threshold Optical Parametric Oscillator, *Phys. Rev. Lett.* **97**, 140504 (2006).
- [6] K. N. Cassemiro, A. S. Villar, P. Valente, M. Martinelli, and P. Nussenzveig, Experimental observation of three-color optical quantum correlations, *Opt. Lett.* **32**, 695 (2007).
- [7] W. P. Bowen, N. Treps, B. C. Buchler, R. Schnabel, T. C. Ralph, H.-A. Bachor, T. Symul, and P. K. Lam, Experimental investigation of continuous-variable quantum teleportation, *Phys. Rev. A* **67**, 032302 (2003).
- [8] N. Treps, N. Grosse, W. P. Bowen, C. Fabre, H.-A. Bachor, and P. K. Lam, A quantum laser pointer, *Science* **301**, 940 (2003).
- [9] N. C. Menicucci, S. T. Flammia, and O. Pfister, One-Way Quantum Computing in the Optical Frequency Comb, *Phys. Rev. Lett.* **101**, 130501 (2008).
- [10] M. Pysher, Y. Miwa, R. Shahrokhshahi, R. Bloomer, and O. Pfister, Parallel Generation of Quadripartite Cluster Entanglement in the Optical Frequency Comb, *Phys. Rev. Lett.* **107**, 030505 (2011).
- [11] M. Chen, N. C. Menicucci, and O. Pfister, Experimental Realization of Multipartite Entanglement of 60 Modes of a Quantum Optical Frequency Comb, *Phys. Rev. Lett.* **112**, 120505 (2014).
- [12] C. H. Monken, P. H. Souto Ribeiro, and S. Pádua, Transfer of angular spectrum and image formation in spontaneous parametric down-conversion, *Phys. Rev. A* **57**, 3123 (1998).
- [13] P. G. Kwiat, E. Waks, A. G. White, I. Appelbaum, and P. H. Eberhard, Ultrabright source of polarization-entangled photons, *Phys. Rev. A* **60**, R773(R) (1999).
- [14] P. G. Kwiat, Hyper-entangled states, *J. Mod. Opt.* **44**, 2173 (1997).
- [15] M. F. Santos, P. Milman, A. Z. Khoury, and P. H. Souto Ribeiro, Measurement of the degree of polarization entanglement through position interference, *Phys. Rev. A* **64**, 023804 (2001).
- [16] D. P. Caetano, P. H. Souto Ribeiro, J. T. C. Parda, and A. Z. Khoury, Quantum image control through polarization entanglement in parametric down-conversion, *Phys. Rev. A* **68**, 023805 (2003).

- [17] J. T. Barreiro, T.-C. Wei, and P. G. Kwiat, Remote Preparation of Single-Photon “hybrid” Entangled and Vector-Polarization States, *Phys. Rev. Lett.* **105**, 030407 (2010).
- [18] A. Mair, A. Vaziri, G. Weihs, and A. Zeilinger, Entanglement of the orbital angular momentum states of photons, *Nature (London)* **412**, 313 (2001).
- [19] D. P. Caetano, M. P. Almeida, P. H. Souto Ribeiro, J. A. O. Huguenin, B. Coutinho dos Santos, and A. Z. Khoury, Conservation of orbital angular momentum in stimulated down-conversion, *Phys. Rev. A* **66**, 041801(R) (2002).
- [20] W. T. Buono, L. F. C. Moraes, J. A. O. Huguenin, C. E. R. Souza, and A. Z. Khoury, Arbitrary orbital angular momentum addition in second harmonic generation, *New J. Phys.* **16**, 093041 (2014).
- [21] L. J. Pereira, W. T. Buono, D. S. Tasca, K. Dechoum, and A. Z. Khoury, Orbital-angular-momentum mixing in type-ii second-harmonic generation, *Phys. Rev. A* **96**, 053856 (2017).
- [22] W. T. Buono, J. Santiago, L. J. Pereira, D. S. Tasca, K. Dechoum, and A. Z. Khoury, Polarization-controlled orbital angular momentum switching in nonlinear wave mixing, *Opt. Lett.* **43**, 1439 (2018).
- [23] R. F. Offer, A. Daffurn, E. Riis, P. F. Griffin, A. S. Arnold, and S. Franke-Arnold, Gouy phase-matched angular and radial mode conversion in four-wave mixing, *Phys. Rev. A* **103**, L021502 (2021).
- [24] G.-L. Oppo, M. Brambilla, and L. A. Lugiato, Formation and evolution of roll patterns in optical parametric oscillators, *Phys. Rev. A* **49**, 2028 (1994).
- [25] M. Marte, H. Ritsch, K. I. Petsas, A. Gatti, L. A. Lugiato, C. Fabre, and D. Leduc, Spatial patterns in optical parametric oscillators with spherical mirrors: classical and quantum effects: errata, *Opt. Express* **3**, 476 (1998).
- [26] C. Schwob, P. Cohadon, C. Fabre, M. Marte, H. Ritsch, A. Gatti, and L. Lugiato, Transverse effects and mode couplings in opos, *Appl. Phys. B* **66**, 685 (1998).
- [27] R. F. Barros, G. B. Alves, and A. Z. Khoury, Gouy-phase effects in the frequency combs of an optical parametric oscillator, *Phys. Rev. A* **103**, 023511 (2021).
- [28] M. Martinelli, J. A. O. Huguenin, P. Nussenzveig, and A. Z. Khoury, Orbital angular momentum exchange in an optical parametric oscillator, *Phys. Rev. A* **70**, 013812 (2004).
- [29] B. C. dos Santos, A. Z. Khoury, and J. A. O. Huguenin, Transfer of orbital angular momentum in a multimode parametric oscillator, *Opt. Lett.* **33**, 2803 (2008).
- [30] G. B. Alves, R. F. Barros, D. S. Tasca, C. E. R. Souza, and A. Z. Khoury, Conditions for optical parametric oscillation with a structured light pump, *Phys. Rev. A* **98**, 063825 (2018).
- [31] A. Aadhi, G. K. Samanta, S. C. Kumar, and M. Ebrahim-Zadeh, Controlled switching of orbital angular momentum in an optical parametric oscillator, *Optica* **4**, 349 (2017).
- [32] M. J. Padgett and J. Courtial, Poincaré-sphere equivalent for light beams containing orbital angular momentum, *Opt. Lett.* **24**, 430 (1999).
- [33] B. C. dos Santos, C. E. R. Souza, K. Dechoum, and A. Z. Khoury, Phase conjugation and adiabatic mode conversion in a driven optical parametric oscillator with orbital angular momentum, *Phys. Rev. A* **76**, 053821 (2007).
- [34] R. Rodrigues, J. Gonzales, B. P. da Silva, J. Huguenin, M. Martinelli, R. M. de Araújo, C. Souza, and A. Khoury, Orbital angular momentum symmetry in a driven optical parametric oscillator, *Opt. Lett.* **43**, 2486 (2018).
- [35] A. G. de Oliveira, M. F. Z. Arruda, W. C. Soares, S. P. Walborn, A. Z. Khoury, A. Kanaan, P. H. S. Ribeiro, and R. M. de Araújo, Phase conjugation and mode conversion in stimulated parametric down-conversion with orbital angular momentum: a geometrical interpretation, *Braz. J. Phys.* **49**, 10 (2019).
- [36] M. Lassen, G. Leuchs, and U. L. Andersen, Continuous Variable Entanglement and Squeezing of Orbital angular Momentum States, *Phys. Rev. Lett.* **102**, 163602 (2009).
- [37] B. C. dos Santos, K. Dechoum, and A. Z. Khoury, Continuous-Variable Hyperentanglement in A Parametric Oscillator with Orbital Angular Momentum, *Phys. Rev. Lett.* **103**, 230503 (2009).
- [38] K. Liu, J. Guo, C. Cai, S. Guo, and J. Gao, Experimental Generation of Continuous-Variable Hyperentanglement in an Optical Parametric Oscillator, *Phys. Rev. Lett.* **113**, 170501 (2014).
- [39] C. Cai, L. Ma, J. Li, H. Guo, K. Liu, H. Sun, and J. Gao, Experimental characterization of continuous-variable orbital angular momentum entanglement using stokes-operator basis, *Opt. Express* **26**, 5724 (2018).
- [40] A. Pecoraro, F. Cardano, L. Marrucci, and A. Porzio, Continuous-variable entangled states of light carrying orbital angular momentum, *Phys. Rev. A* **100**, 012321 (2019).
- [41] L. Ma, H. Guo, H. Sun, K. Liu, B. Su, and J. Gao, Generation of squeezed states of light in arbitrary complex amplitude transverse distribution, *Photon. Res.* **8**, 1422 (2020).
- [42] A. Siegman, *Lasers* (University Science Books, Sausalito, CA, 1986).